



# Preparation of PPy/TiO<sub>2</sub> core-shell nanorods film and its photocathodic protection for 304 stainless steel under visible light

Yunpeng Liu<sup>a,1</sup>, Chengcheng Zhao<sup>a,1</sup>, Xi Wang<sup>a</sup>, Hao Xu<sup>a</sup>, Hui Wang<sup>a</sup>, Xuyang Zhao<sup>a</sup>, Jiangtao Feng<sup>a,\*</sup>, Wei Yan<sup>a,\*</sup>, Zijun Ren<sup>b</sup>

<sup>a</sup> Department of Environmental Science & Engineering, State Key Laboratory of Multiphase Flow in Power Engineering, Xi'an Jiaotong University, Xi'an, 710049, China

<sup>b</sup> Instrument Analysis Center of Xi'an Jiaotong University, Xi'an Jiaotong University, Xi'an, 710049, China

## ARTICLE INFO

### Keywords:

TiO<sub>2</sub>  
PPy  
Core-shell structure  
304SS  
Photocathodic protection

## ABSTRACT

In this study, polypyrrole (PPy)/TiO<sub>2</sub> core-shell nanorods (PTNRs) films were successfully synthesized through hydrothermal treatment and electrochemical polymerization method. The structure and optical properties of the as-prepared films were characterized. The results showed that the core-shell PTNRs film exhibits superior visible-light absorption ability. The composite films with different deposition conditions were systematically studied on the performance of the photocathodic protection (PCP). The photoelectrochemical performance of the samples are related to their structures which are strongly influenced by the deposition time of PPy layer. Meanwhile, compared with other reported as-prepared films, PTNRs film under visible light illumination could negatively shift the potential of the coupled 304 stainless steel (304SS) to -640 mV vs. Ag/AgCl, exhibiting more efficient PCP effect. More importantly, it can continuously provide protection for the steel in the darkness based on the electron pool effect of PPy. The possible PCP mechanism of PTNRs film was also discussed.

## 1. Introduction

304SS is extensively used as metallic bulks in industrial applications based on its good corrosion resistance property. However, localized corrosion distributed on the bulks is hardly to avoid in marine environments [1]. Recently, many methods have been developed to inhabit this corrosion problem, including anticorrosion coatings [2], corrosion inhibitors [3], electrochemical protection [4], etc. Among these methods, building photocathodic protection (PCP) is generally regarded as the most effective way, which can be successfully conducted without non-regenerate energy nor extra material consumption. During that process, the semiconductor is served as the photoanode [5] which can produce photogenerated electrons. The photogenerated electrons are then transferred to the coupled metal, shifting its metal surface potential. When the surface potential of metal drops lower than its corrosion potential [6], metal corrosion can be inhibited.

As one of most widely used semiconductor materials, TiO<sub>2</sub> has been frequently studied as photoanodes in the PCP system due to its low cost, low toxicity and high chemical stability [7]. Research shows that one-dimensional (1D) electron transmission can decrease the recombination of photogenerated electron/hole (e<sup>-</sup>/h<sup>+</sup>) pairs [8]. Thus 1D TiO<sub>2</sub> array

films, including nanotubes (TNTs) films [9], nanowires or nanorods (TNRs) films [10,11], exhibit better PCP performances than the TiO<sub>2</sub> nanoparticles film. However, there are two serious defects of practical TNTs films: (i) the formation process of TNTs could cause F<sup>-</sup> ions pollution [12] (ii) as a traditional polycrystalline TiO<sub>2</sub> [13], the application of TNTs is limited due to the severe electron scattering and its trapping at grain boundaries [14,15]. In order to overcome those shortages of TNTs, the research focus turns to the TNRs film, since the single crystalline rutile TNRs with much less lattice defects can improve the mobility efficiency of charges and its synthesis do not release any pollution as well [14]. Liu et al. [16] synthesized the single crystalline rutile TNRs onto fluorine-doped tin oxide (FTO) glass for the first time and studied its photoelectric properties as dye sensitized solar cells. Various applications of single crystalline rutile TNRs film were further investigated, particularly including PCP applications [17,18]. Although the band-gap energy (E<sub>g</sub>) of rutile TiO<sub>2</sub> (3.0 eV) is narrower than that of anatase TiO<sub>2</sub> (3.2 eV) [19], its relatively wide band gap limits its PCP response under visible light illumination. Additionally, it is also a challenge for the pure TNRs film to provide continuous cathodic protection effect of metals in the dark [20]. At present, combinations between TNRs and other semiconductor materials (such as SnO<sub>2</sub> [21],

\* Corresponding authors.

E-mail addresses: [fjtes@xjtu.edu.cn](mailto:fjtes@xjtu.edu.cn) (J. Feng), [yanwei@xjtu.edu.cn](mailto:yanwei@xjtu.edu.cn) (W. Yan).

<sup>1</sup> These authors contributed equally to this work.

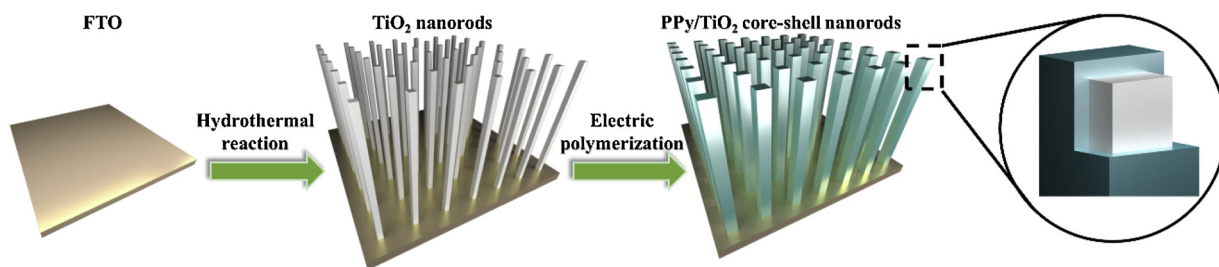


Fig. 1. Diagram of the synthesis process for the TiO<sub>2</sub> nanorods film and PPy/TiO<sub>2</sub> core-shell nanorods film.

WO<sub>3</sub> [22], CdSe [23], etc.) are often used to deal with those problems.

PPy, a stable, nontoxic, and superior-conductivity polymer, has been more and more used to compound with TiO<sub>2</sub> because of its narrow band gap and good reversible doping-dedoping capacity [24]. The PPy/TiO<sub>2</sub> p-n heterojunctions have been reported in some researches about applications in PCP systems [25,26]. Working as PPy/TiO<sub>2</sub> photoanode, PPy (2.2 eV) can be excited to generate e<sup>-</sup> under visible light illumination, and then injecting e<sup>-</sup> into the conduct band (CB) of TiO<sub>2</sub> to promote the separation of e<sup>-</sup>/h<sup>+</sup> pairs, ultimately leading to the increase of cathodic protection efficiency. Additionally, PPy can also be regarded as an electron pool to storage and release e<sup>-</sup> in the hybrid system [27], and provide sustaining protection for the steel under darkness. Cui et al. [25] and Ren et al. [26] have also synthesized the PPy/TNTs composite film with favourable cathodic protection performance. In conclusion, there is a reason to speculate that as a superior replacement materials of TNTs film, the PPy/TNRs composite film may have greater value in the field of PCP applications.

Compared with traditional PPy/TNRs composite film, the PPy/TNRs core-shell nanorods film exhibit better photosensitivity performance [28,29]. Under the premise of the sufficient load of PPy, the core-shell structure can maintain the 1D electron transmission shortcut of TNRs and provide a large area for the p-n interface, thus, decrease the recombination of e<sup>-</sup>/h<sup>+</sup> pairs in theory [30–32]. Meanwhile, the electropolymerization deposition of PPy layer is faster and easier to control than other methods, such as chemical polymerization and UV-light photopolymerization, and can also effectively avoid the formation of excess-loading thick PPy film [27]. Thus, it's of great value to optimize the electropolymerization method of the preparation of PTNRs composite film in order to develop the cathodic protection of steel. However, at present there are few reports on the synthesis and PCP-application of this composite film.

In this work, the PTNRs composite films were synthesized onto the conductive FTO glass substrate via hydrothermal treatment and electrochemical deposition method, and their PCP performances and protection mechanism for 304SS were systematically investigated.

## 2. Materials and methods

### 2.1. Chemicals

The detailed information of all the chemicals are listed in the Table S1. Typically, pyrrole was freshly distilled and then stored under the aerated nitrogen condition in a refrigerator (0 °C) before used. Distilled water (DIW) was used for the preparation of all solutions in this study.

FTO glass (7 Ω·cm<sup>-2</sup>, 2.2 mm-thick) was purchased from Guluo Glass Co. Ltd, (Luoyang, China). Before the experiment, the FTO structure was treated by ultrasonic cleaning in DIW, followed by acetone and alcohol for 30 min each. Finally, these glass were dried in ambient air.

### 2.2. Synthesis of PTNRs composite films

#### 2.2.1. Preparation of TNRs film

The TNRs array film was synthesized on FTO glass via the hydrothermal method using the following procedure [33]. Firstly, 60 mL of HCl aqueous solution (6 mol·L<sup>-1</sup>) mixed with 1.0 mL C<sub>16</sub>H<sub>36</sub>O<sub>4</sub>Ti was transferred into a Teflon-lined stainless steel autoclave (100 mL). Then a piece of FTO glass was placed at an angle (60 °) against the wall of the above autoclave with the conducting side facing down, and being heated at 150 °C for 10 h in an electric oven. After the reaction, the sample was rinsed with DIW, and then calcined in a muffle furnace at 500 °C for 2 h to enhance the contact between the TNRs and the FTO substrate.

#### 2.2.2. Preparation of PTNRs film

The pyrrole monomer was electrochemically polymerized onto the surface of TNRs via a potentiostatic method on a CHI660D electrochemical workstation (Shanghai Chinstrument Co., Ltd, China). In a three electrode system, TNRs array film, Ag/AgCl electrode and Pt foil were served as the work electrode (WE), the reference electrode (RE) and the counter electrode (CE), respectively, and the aqueous electrolyte consisted of 0.1 mol·L<sup>-1</sup> H<sub>2</sub>SO<sub>4</sub> and 0.01 mol·L<sup>-1</sup> pyrrole. The electropolymerization process was conducted potentiostatically at 0.8 V for 20 min under ambient condition. Afterwards, the as-prepared film was washed with DIW and dried overnight in a vacuum drying oven at 50 °C. To compare the PCP performances of PTNRs film and the other PPy/TNRs composite films with different structure, the PPy/TNRs composite films with different electropolymerization time (10 min and 30 min) was also synthesized according to the method mentioned above, denoting as PPy/TNRs-10 and PPy/TNRs-30, respectively. A schematic diagram for constructing these composites is shown in Fig. 1.

### 2.3. Characterizations

The morphology and microstructure of as-prepared samples were investigated by scanning electron microscope (SEM Zeiss Gemini SEM 500) and field emission transmission electron microscopy (TEM, JEOL JEM-F200 (HR)). The film compositions were detected by energy dispersive x-ray spectroscopy (EDS) elemental mapping. The x-ray diffraction (XRD) patterns of samples were recorded on a Bruker D8 ADVANCE using a Cu Kα radiation (λ = 1.5418 Å). The Raman measurement (LabRAM HR Evolution, with an excitation of 325 nm laser light) was used to analyze the composition of the samples. The X-ray photoelectron spectroscopy (XPS) spectrum of samples was performed on Thermo Scientific EscaLab 250Xi with an Al monochromatic X-ray source (1486.6 eV), and all binding energies (BEs) were referenced to the C 1s hydrocarbon peak at 284.8 eV. The optical absorption ability of the samples was investigated by UV-vis diffuse reflectance absorption spectrum (DRS, PE Lambda950). The photoluminescence (PL) spectra were studied using an Edinburgh FLS9 luminescence spectrofluorophotometer equipped with a Xe lamp presenting an excited wavelength at 330 nm.

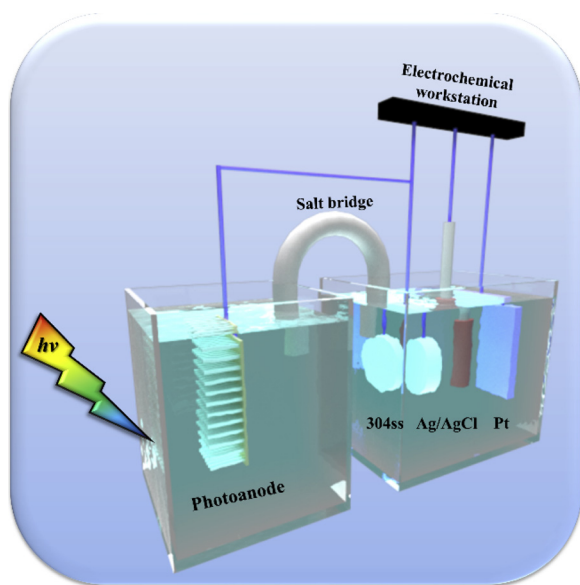


Fig. 2. Schematic of photoelectrochemical test device.

#### 2.4. Photoelectrochemical tests

As shown in Fig. 2, all the photoelectrochemical tests were performed on the CHI660D electrochemical workstation using a double electrolytic cell setup, which consisted of a corrosion cell (3.5 wt% NaCl solution) and a photoelectrochemical cell ( $0.1 \text{ mol}\cdot\text{L}^{-1} \text{ Na}_2\text{S} + 0.2 \text{ mol}\cdot\text{L}^{-1} \text{ NaOH}$  mixed solution), and the two couple cells were connected by a U-type salt bridge (a flexible glass tube with  $1.0 \text{ mol}\cdot\text{L}^{-1} \text{ KCl}$  in agar). In the corrosion cell, a traditional conventional three-electrode system was used, in which the 304SS electrode, Ag/AgCl electrode and Pt foil were served as the WE, RE and CE, correspondingly. Meanwhile, the as-prepared film was immersed in photoelectrochemical cell electrolyte as the photoanode, which was connected with the 304SS by a copper wire. Electrochemical measurements were investigated under intermittent visible light ( $100 \text{ mW}\cdot\text{cm}^{-2}$ ) supplied by a 500 W xenon lamp (CHF-XM-500W, Beijing Changtuo technology Co., Ltd. Beijing, China) equipped with the UV cut-off filter ( $\lambda > 420 \text{ nm}$ ). The open circuit potentials (OCP) and Tafel curves were tested with the scanning rate of  $1 \text{ mV/s}$ , and the photocurrent density of the sample was detected without any applied bias voltage. When the OCPs of the samples keep nearly constant, the electrochemical impedance spectroscopy (EIS) was tested at OCP over a frequency range of  $10^5$  to  $10^{-2} \text{ Hz}$  with a  $10 \text{ mV}$  AC amplitude. The efficient area of 304SS and as-prepared samples was  $1 \text{ cm}^2$ , and the 304SS was ground with abrasive paper before these experiment. All the photoelectrochemical tests were not be performed until the measurement system reach a relatively stable state.

### 3. Results and discussion

#### 3.1. Structural characteristics

The Raman spectra for the TNRs and PTNRs films were measured to confirm the compositions of the composite films. As shown in Fig. 3a, the curve of TNRs shows three strong characteristic peaks at about  $234$ ,  $447$  and  $601 \text{ cm}^{-1}$ , corresponding to the  $B_{1g}$ ,  $E_g$ ,  $A_{1g}$  modes of rutile  $\text{TiO}_2$ , respectively [34]. Meanwhile, there is no characteristic Raman peak of anatase  $\text{TiO}_2$  [35], which indicates that the single crystalline rutile TNRs is synthesized after 10 h hydrothermal reaction. From the curve of pure PPy, the main Raman bands at  $1584 \text{ cm}^{-1}$  is assigned to CC= backbone stretching vibration, and the absorption peaks at  $1389 \text{ cm}^{-1}$  and  $1322 \text{ cm}^{-1}$  are ascribed to CN and CH— of pyrrole ring

stretching vibrations, respectively [36]. Absorption peaks at  $1052$ ,  $971$  and  $928 \text{ cm}^{-1}$  are related to the ring deformation vibration [37]. After the deposition of PPy layer on the TNRs film, the characteristic Raman peaks of rutile  $\text{TiO}_2$  and PPy can be both observed. This result confirms that the PPy layer is successfully deposited on the surface of nanorods through the potentiostatic polymerization process.

The XRD patterns of TNRs and PTNRs films were used to investigate the crystal phases and compositions, as shown in Fig. 3b. The diffraction peaks of the TNRs at  $27.5^\circ$ ,  $36.2^\circ$ ,  $41.3^\circ$ ,  $62.9^\circ$ ,  $69.2^\circ$  and  $70.0^\circ$  are well matched with the (1 1 0), (1 0 1), (1 1 1), (0 0 2), (3 0 1) and (1 1 2) planes of rutile  $\text{TiO}_2$  (JCPDS # 65-0912), respectively, showing the TNRs are highly crystallized [38]. Other indifferent peaks, such as  $25.6^\circ$ ,  $33.9^\circ$ ,  $37.8^\circ$  and  $51.6^\circ$ , are derived from the FTO substrate. After the electropolymerization of PPy layer on the surface of TNRs, all the relative characteristic XRD peaks of rutile  $\text{TiO}_2$  in PTNRs weakens to some extent, resulting from screening effect of the amorphous PPy [39]. This further proofs the presence of PPy layer on the single crystalline rutile TNRs film.

SEM images with two different magnifications of TNRs and PTNRs films are shown in Fig. 4. As previously reported [40], the TNRs grew densely and uniformly on FTO substrate (Fig. 4a). In the high magnification SEM image of TNRs (Fig. 4b), the average diameter of TNRs is approximately  $150 \text{ nm}$ . The cross-section image (Fig. 4c) of the TNRs shows that the nanorods are  $5.27 \mu\text{m}$  high on average and are nearly vertical to the FTO substrate along the [0 0 1] direction. With the electropolymerization of PPy layer on the surface of  $\text{TiO}_2$  nanorod, the color of the substrate turns from white to black (inset of Fig. 4a and b). PTNRs becomes relatively compact compared with the TNRs (Fig. 4c and d), and the average width of the nanorods increases to around  $170 \text{ nm}$  after being deposited for 20 min. Meanwhile, the 1D electron transmission shortcut of nanorods has not been destroyed (Fig. 4f), as it is shown in the picture, the composite nanorods increase in diameter after the deposition.

The microstructure and the crystal structure of PTNRs film were further characterized by TEM and high-resolution TEM (HRTEM), as shown in Fig. 5. After the electropolymerization of pyrrole monomer for 20 min, the PPy layer is uniformly formed on the surface of TNRs (Fig. 5a and b), and the diameter of the compound nanorod is around  $180 \text{ nm}$ . Also, from the picture, it can be seen that the core-shell structure heterojunction is formed. The interface of the TNRs and PPy layer clearly displays, where the rutile TNRs acts as the core and the external covering PPy layer acts as the shell. The average thickness of the PPy shell is  $\sim 13.02 \text{ nm}$  (Fig. 5c), which is consistent with the SEM result discussed above. As shown in Fig. 5d, the lattice fringes can be assigned to the interplaner spacing of rutile  $\text{TiO}_2$  (1 1 0) ( $d_{110} = 3.2 \pm 0.1 \text{ \AA}$ ), and the [0 0 1] direction is vertical against the nanorod. Therefore, it can be indicated that TNRs, the core of the PTNRs, grows along the [0 0 1] direction. The inset of Fig. 5d shows the selected-area electron diffraction pattern, signifying that the nanorod in the PTNRs composite film is single crystalline rutile  $\text{TiO}_2$ . The EDS elemental mappings (Fig. S1) reveals the obvious core-shell structure, the core of the nanorod is TNRs and edge part of the nanorod covered with PPy layer.

XPS analysis of the TNRs and PTNRs film is shown in Fig. 6, which can be employed to the further investigation of chemical composition. Fig. 6a displays the XPS spectrum of the PTNRs film over a large energy range at low resolution, showing Ti 2p, C 1s, N 1s and S 2p peaks in the sample without any obvious impurities. According to Fig. 6b, The Ti 2p spectra of TNRs and PTNRs films includes two types:  $\text{Ti } 2p_{3/2}$  and  $\text{Ti } 2p_{1/2}$  [41]. After the deposition of PPy layer, Ti 2p peaks of PTNRs shift relatively to those of TNRs, indicating that TNRs may have an interaction with PPy layers [42]. As shown in the high resolution XPS spectrum of O 1s (Fig. 6b), there exist two strong peaks, a dominate peak at  $530.0 \text{ eV}$  and a shoulder peak at  $532.3 \text{ eV}$ , corresponding to the lattice oxygen (O—Ti) of  $\text{TiO}_2$  and surficial hydroxyl groups (OH—), respectively [43]. As presented in high resolution XPS spectrum of C 1s



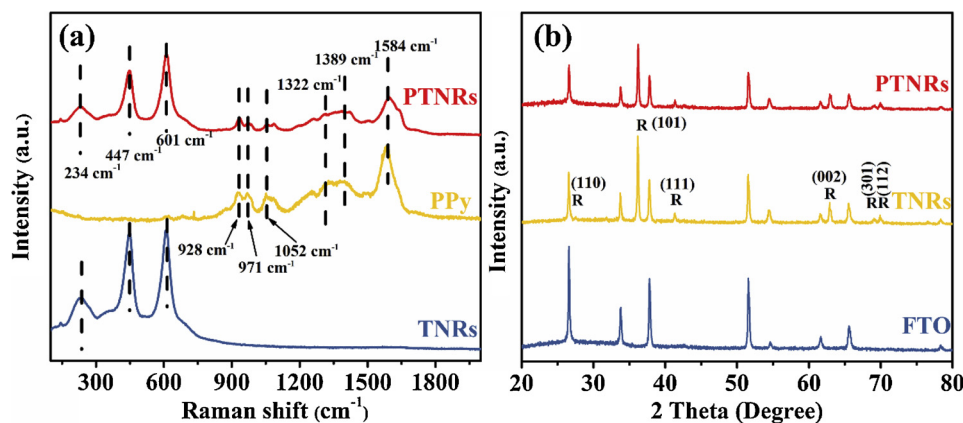


Fig. 3. (a) The Raman spectra for the TNRs, PPy and PTNRs and (b) the XRD patterns of FTO glass, TNRs and PTNRs.

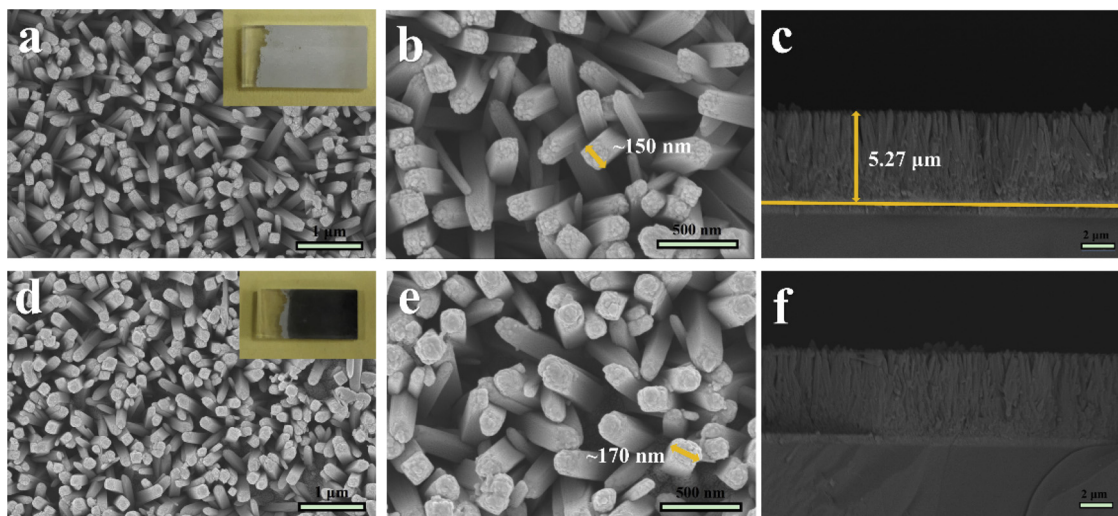


Fig. 4. Top-view and cross-view SEM images of the TNRs (a, b and c) and PTNRs (d, e and f), and their macroscopic appearances of the substrate (inset).

(Fig. 6c), three peaks at 284.8, 286.1 and 288.6 eV are assigned to C–C/CH, CN and CO—, respectively [42]. Fig. 6d exhibits the high resolution XPS spectrum of N 1s. A dominant peak at 401.6 eV and two shoulder peaks at 402.4 and 400.0 eV, appear after curve fitting, which can be assigned to the neutral pyrrolylium nitrogen (–NH), the positively charged nitrogen atom (N–<sup>+</sup>) and the imine nitrogen atom (=N)– in the given order [44]. The presence of N<sup>+</sup> implies that PPy is in the oxidized state. Based on the fitting areas of the three peaks of N 1s, the N<sup>+</sup> ratio is approximately 8.4 %, indicates the stable electrical conductivity of PPy layer. In a word, PPy layer displays the excellent conductivity property in the existence of N<sup>+</sup> polarons, which can transfer electrons directly via the electrostatic interaction and promote the charge transfer between PPy layer and TNRs accordingly.

In order to investigate the optical properties of TNRs and PTNRs films, the UV–vis DRS spectra and  $(\alpha h\nu)^2$  versus  $h\nu$  plots are presented in Fig. 7. Compared with TNRs film, PTNRs film exhibits much stronger absorption shoulder in visible light region (400–600 nm), the red shift of the absorption edge to longer wavenumber region can be obviously observed. Meanwhile, in order to obtain  $E_g$  of the as-prepared film, the Tauc plot is calculated according to the following equation [45].

$$\alpha h\nu = A(h\nu - E_g)^n \quad (1)$$

where  $\alpha$ ,  $h$ ,  $\nu$ ,  $A$ , and  $n$  represents optical absorption coefficient, Planck constant, light frequency, a constant and the quantum efficiency in turn. For rutile TiO<sub>2</sub>, the value of  $n$  is set as 1/2 as a direct semiconductor [46]. The plots of  $(\alpha h\nu)^2$  vs.  $h\nu$  for the as-prepared films are displayed in Fig. 7b. The  $E_g$  can be obtained via extrapolating the linear

part of the curve to  $\alpha = 0$ . The measured  $E_g$  of PTNRs composite is narrowed to be about 2.97 eV, while that of the pure TNRs is 3.10 eV as previously reported [47]. The results reveal that the core-shell structure of PTNRs can significantly enhance the visible light adsorption ability and thus improve the photoelectrochemical effect of the composite film, and promote its PCP properties for 304SS.

Fig. 8 displays the PL spectra of TNRs and PTNRs films using excited wavelength at 330 nm. The PL emission spectrum of TNRs shows four main peaks at 408, 428, 456 and 475 nm, separately. The emission peak at 408 nm results from phonon assisted indirect transition from edge ( $\chi$ ) to the center ( $\Gamma$ ) of the Brillouin zone, while the peak at around 428 nm is related to trapped electrons recombined with holes inside the bulk lattice of TiO<sub>2</sub> [48]. Whereas the emission peak at 456 nm is due to the recombination of e<sup>−</sup> with surface oxygen defects. Besides, the emission peak at around 475 nm is due to charge transfer from Ti<sup>3+</sup> to TiO<sub>6</sub><sup>2−</sup> octahedra [49]. Nonetheless, only the bulk e<sup>−</sup>-h<sup>+</sup> recombination with the peak at 428 nm is harmful to the photoelectron activity [50]. By comparing the relative intensities of the four main contributions (listed in Table 1), it's obvious that only the bulk e<sup>−</sup>-h<sup>+</sup> shows the recombination peak at 428 nm of composite film, exhibiting a decreased relative intensity after the deposition of PPy layer, while the peak intensities of recombination with surface oxygen defects and charge transfer from Ti<sup>3+</sup> to TiO<sub>6</sub><sup>2−</sup> octahedra have no significant changes. In other words, the recombination of e<sup>−</sup>-h<sup>+</sup> pairs in this composite film is markedly restrained via the deposition of PPy layer on the TiO<sub>2</sub> nanorod. Therefore, the PTNRs film with core-shell structure may have an excellent effect in PCP practice for 304SS comparing with

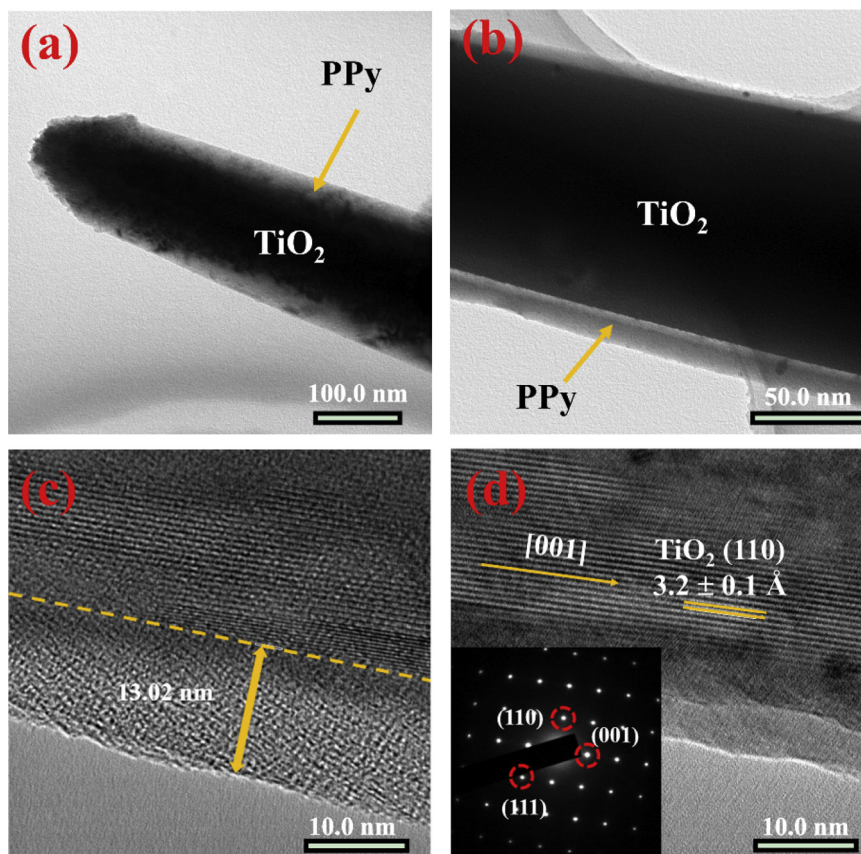


Fig. 5. TEM images (a and b) and HRTEM images of PTNRs (c and d). Inset image of (d) is the SAED pattern of the composite film.

the pure TNRs film.

### 3.2. Photoelectrochemical properties of TNRs and PTNRs film

The principle of PCP is mainly based on the transfer of

photoinduced electrons. When  $e^-$  is excited from photoanode and immigrated to the connected metal electrode, this metal is protected from being corroded [9]. Fig. 9a exhibits a comparison of the photoinduced current density curves of the TNRs, PTNRs, PPy/TiO<sub>2</sub>-10, and PPy/TiO<sub>2</sub>-30 composite films coupled with 304SS under intermittent visible

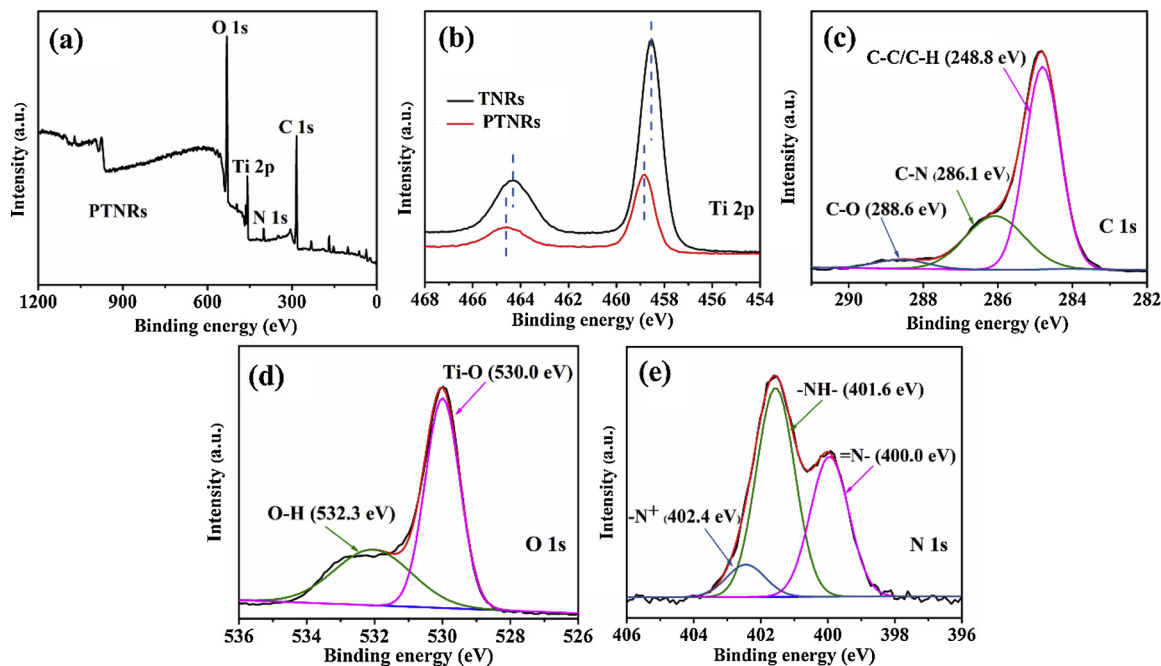


Fig. 6. Full scan survey XPS spectrum (a) and high resolution spectra of (c) O 1s, (d) C 1s and (e) N 1s of PTNRs composite film, and the XPS comparison spectrum of Ti 2p (b) of TNRs and PTNRs films.

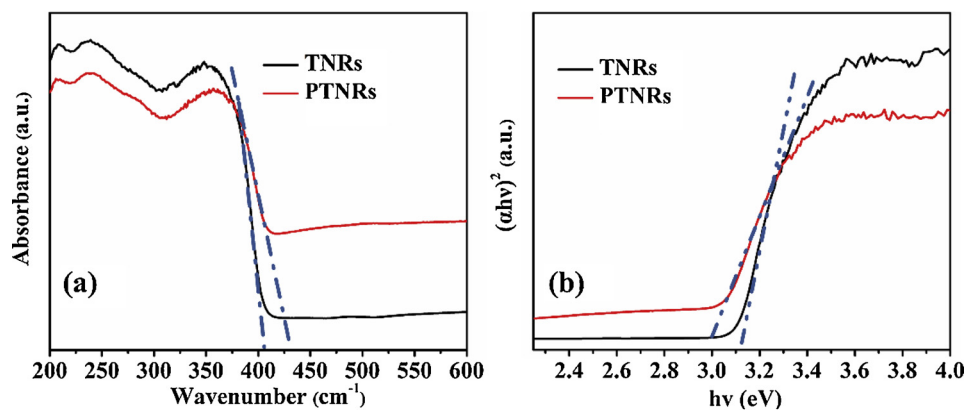


Fig. 7. (a) UV-vis absorption spectra and (b) the plots of  $(\alpha h\nu)^2$  versus  $h\nu$  for the TNRs and PTNRs films.

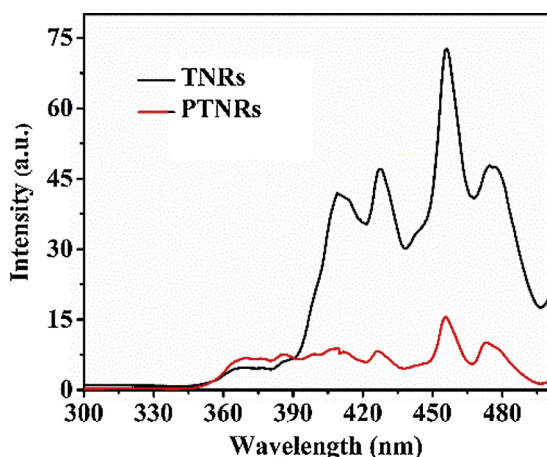


Fig. 8. PL spectra of TNRs and PTNRs films.

Table 1

Relative intensity of the different PL signals for TNRs and PTNRs films.

Samples	Relative Intensity of PL signals (%)			
	408 nm	428 nm	456 nm	475 nm
TNRs	100	112	173	114
PTNRs	100	91.8	170	114

light illumination. As can be seen, curves of the PPy/TiO<sub>2</sub> composite films display higher photoelectric sensitivities than the pure TNRs film, which can be ascribed to the formation of p-n heterojunction between PPy and TiO<sub>2</sub>. With visible light irradiation, the excited e<sup>-</sup> from the highest occupied molecular orbital (HOMO) to the lowest unoccupied molecular orbital (LUMO) of PPy can be directly transferred to the relatively more positive CB of TiO<sub>2</sub>, resulting in the higher charge separation efficiencies. Meanwhile, the PTNRs film exhibits a highest photocurrent density (28  $\mu\text{A cm}^{-2}$ ) than the other composite films, attributing to its core-shell structure. With the support of the sufficient deposition of PPy layer, the coaxial nanorod structure can provide shorter e<sup>-</sup> migration path which can favor the immigration and separation efficiency [51]. With regard to PPy/TiO<sub>2</sub>-10 and PPy/TiO<sub>2</sub>-30 composite films, samples coated with lower or higher PPy show smaller photoelectric response. As shown in Fig. S2a, on the surface of TNRs covered with excessively thick PPy layer formed by PPy/TiO<sub>2</sub>-30 composite films, which may result in low photocurrent density. The over-deposited PPy on the film act as the recombination centers of e<sup>-</sup>/h<sup>+</sup> pairs [52], thus impeding the electrons immigration from the photoanode to 304SS surface. Meanwhile, inadequate deposition of PPy on

TiO<sub>2</sub> nanorod (Fig. S2b) may hinder the formation of the effective p-n heterojunction, causing the low photoelectric sensitivity.

Based on the discussion above, the PTNRs film exhibits superior visible light response and better photoelectrochemical performance than other composite films, which provides a better choice for the PCP application. In order to evaluate the cathodic protection efficiency of as-prepared films on 304SS, the samples (TNRs and PPy/TiO<sub>2</sub> composite films) are used as photoanode in the photo-induced OCP experiment by measuring the surface potential changes of 304SS with visible light irradiation [53,54]. As shown in Fig. 9b, the bare 304SS corrosion potential is around -180 mV vs. Ag/AgCl, and the OCP of 304SS connected with TNRs film drops slightly to negative values (-260 mV vs. Ag/AgCl). However, for PPy/TiO<sub>2</sub> composite films, the OCPs (-370 - -640 mV vs. Ag/AgCl) of 304SS are much more negative than the corrosion potential of 304SS, especially when 304SS is coupled with PTNRs (-640 mV vs. Ag/AgCl). According to the explanations above, the excellent core-shell structure of PTNRs can enhance the charge separation efficiency and suppress the recombination of e<sup>-</sup>/h<sup>+</sup> pairs. More electrons are transferred to the coupled 304SS to reduce the metal surface potential, presenting better PCP performance [55,56]. In addition, when the light source was turned off, the surface potential of 304SS coupled with TNRs film returns quickly to the initial value (around 180 mV vs. Ag/AgCl), implying its inability of providing cathodic protection for 304SS in dark condition. However, it is obvious that the OCPs of 304SS coupled with PPy/TiO<sub>2</sub>-10, PPy/TiO<sub>2</sub>-30 and PTNRs composite films sustain at stable values (around -240, -280 and -310 mV vs. Ag/AgCl, respectively), which are far lower than the 304SS corrosion potential. In other words, PTNRs film can still provide excellent cathodic protection in dark condition, revealing superior delay protection for 304SS when the light is cut off. This phenomenon can be ascribed to the electron pool effect of PPy, and sectional electrons stored by PPy layer according to doping-dedoping mechanism (Fig. S3) [27,57]. In the doping-dedoping process, PPy can store the excess photogenerated electrons for a short time, and then release these electrons back to the coupled 304SS when in darkness. Through comparing with other common photoanodes (as shown in Table 2), this composite film displays excellent anti-corrosion efficiency for 304SS under visible light illumination. Therefore, the PTNRs film can be used as a potential photoanode material in the cathodic protection applications for 304SS.

In order to further evaluate the anticorrosion efficiency of the as-prepared films in PCP system, the Tafel curves of bare 304SS, 304SS coupled with TNRs, and PTNRs were monitored under visible light illumination (Fig. 9c). It can be clearly observed that the corrosion potential of 304SS coupled with the as-prepared films exhibit remarkable negative shift compared with that of bare 304SS (-187 mV vs. Ag/AgCl). And the corrosion potential 304SS coupled with PTNRs film (-645 mV vs. Ag/AgCl) is much more negative than that of 304SS



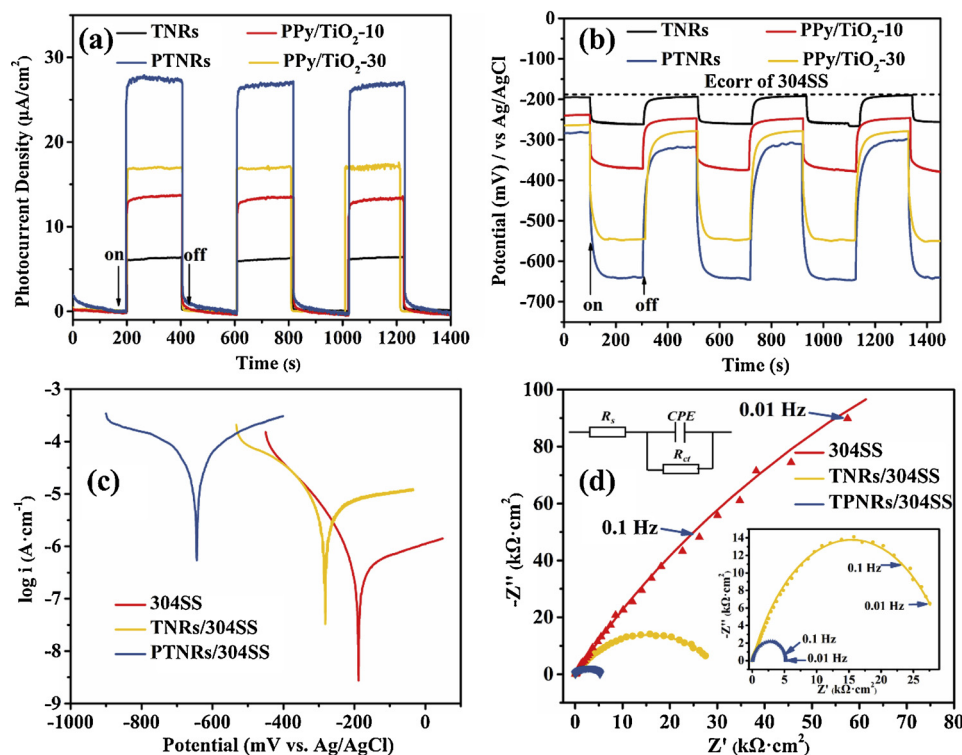


Fig. 9. (a) The photoinduced current density between the as-prepared samples and 304SS under intermittent visible light illumination. (b) The potential change of the 304SS electrodes coupled with the as-prepared films. Polarization curves (c) and Nyquist plots (d) of bare 304SS, and 304SS coupled with TNRs, and PTNRs films electrodes under visible illumination, where the equivalent circuit used to fit the impedance data is also inset in (d).

coupled with TNRs film ( $-282$  mV vs. Ag/AgCl). This result demonstrates that the photoelectric conversion efficiency of PTNRs film is higher than that of TNRs film, and more electrons can be transferred to the surface of 304SS with visible irradiation. By calculating the Tafel curves, the corresponding electrochemical parameters, including corrosion potential ( $E_{corr}$ ), corrosion current ( $j_{corr}$ ), cathodic Tafel slope ( $\beta_c$ ) and anodic Tafel slope ( $\beta_a$ ), are obtained and listed in Table 3. It is well known that the higher  $j_{corr}$  value, the more efficient corrosion resistance will be [63]. The  $j_{corr}$  of PTNRs/304SS is remarkably higher than that of TNRs/304SS and bare 304SS, resulted from the formation of photo-generated charges under visible light illumination. Meanwhile, PTNRs film not only absorbs visible light to generate electrons, but also avoids the recombination of  $e^-/h^+$  pairs with the assistance of the core-shell structure. Based on the above results, the PTNRs film is supposed to exhibit excellent cathodic protection performance for 304SS.

The EIS analysis is an extremely useful tool to explore the corrosion mechanism between the corrosion solution and the metal [64], thus it can be used to investigate the anti-corrosion effect for 304SS in PCP system. Fig. 9d displays the Nyquist plots of the bare 304SS, and 304SS coupled with the as-prepared films (TNRs and PTNRs films) under visible light radiation. Only one impedance arc can be observed from each Nyquist plot, and it can be well fitted in the corresponding equivalent circuit ( $R_s$  (CPE  $R_{ct}$ )) in the inset [65], where  $R_s$  is solution

Table 3

Electrochemical impedance parameters obtained by the Tafel curves of pure 304SS, TNRs/304SS and PTNRs/304SS in 3.5 wt% NaCl solution under visible illumination.

Sample	$E_{corr}$ (mV vs. Ag/AgCl)	$j_{corr}$ ( $\mu A \cdot cm^{-2}$ )	$\beta_c$ (mV·dec <sup>-2</sup> )	$\beta_a$ (mV·dec <sup>-2</sup> )
304SS	-187	0.251	-98.7	398.5
TNRs/304SS	-282	17.27	-142.1	382.7
PTNRs/304SS	-645	110.25	-247.0	217.6

resistance,  $R_{ct}$  and CPE represent the charge transfer resistance and the double layer capacitance of the steel/solution interface, in turn. It is obvious that the arc radius of 304SS coupled with PTNRs film is shorter than that of bare 304SS and the coupled 304SS to PTNRs film. According to the fitting data, the value of  $R_{ct}$  of the 304SS coupled with TNRs film ( $36.74$   $k\Omega \cdot cm^2$ ) is much smaller than the uncoupled 304SS ( $773.6$   $k\Omega \cdot cm^2$ ) because of the transfer of photogenerated electrons from the photoanode to the metal, which means that the corrosion of 304SS can be suppressed by the coupling with TNRs film [66]. Meanwhile, the  $R_{ct}$  value is further decreased to  $5.283$   $k\Omega \cdot cm^2$  when the 304SS is coupled with PTNRs film. It indicates that the charge transfer resistance of 304SS coupled with PTNRs film is lower than that of

Table 2

The PCP efficiency of some photoanodes for 304SS under visible light illumination.

Photoanode	The OCP of 304SS coupled to the corresponding photoanode under visible light illumination	Ref.
ZnO nanorods array film	$-320$ mV vs. SCE	[51]
Iron-cobalt WTiO <sub>2</sub> nanotube photoanode	$-430$ mV vs. SCE	[58]
TiO <sub>2</sub> nanotubes array film	$-440$ mV vs. SCE	[59]
Hierarchical WO <sub>3</sub> /TiO <sub>2</sub> nanotube nanocomposite film	$-520$ mV vs. SCE	[60]
WO <sub>3</sub> /TiO <sub>2</sub> composite film	$-510$ mV vs. SCE	[61]
Sb <sub>2</sub> O <sub>3</sub> modified TiO <sub>2</sub> photoanode	$-390$ mV vs. SCE	[20]
graphene/TiO <sub>2</sub> nanotube nanocomposite film	$-400$ mV vs. SCE	[6]
Hydrogenated TiO <sub>2</sub> nanotube arrays film	$-570$ mV vs. SCE	[62]
Polypyrrole nanowire/TiO <sub>2</sub> nanotube nanocomposites	$-360$ mV vs. SCE	[25]
PPy/TiO <sub>2</sub> core-shell nanorods film	$-640$ mV vs. Ag/AgCl	This work

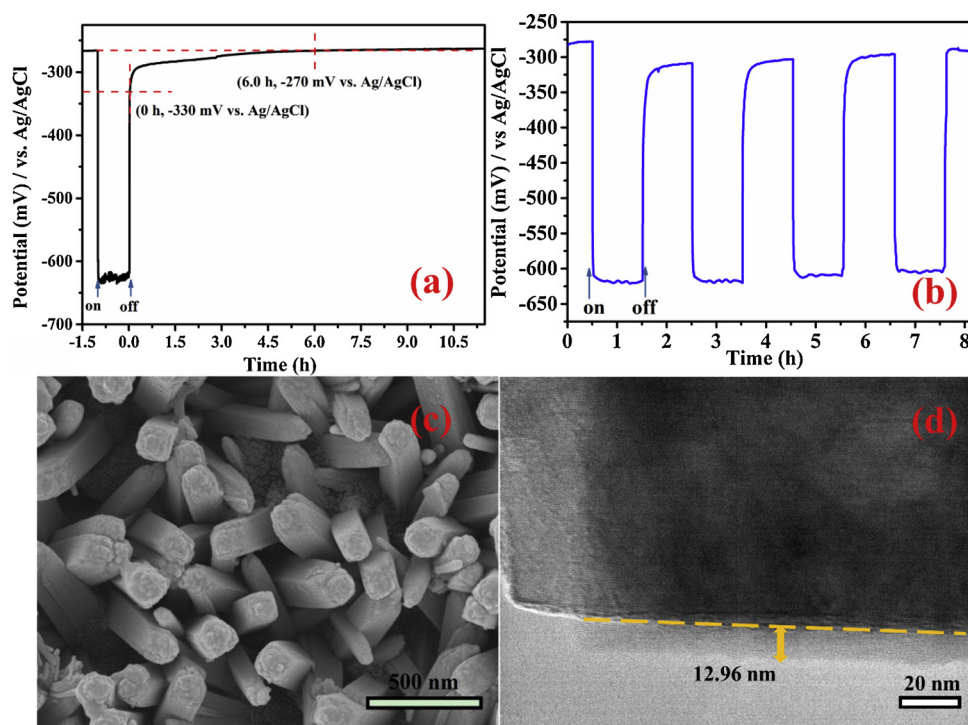


Fig. 10. (a) The potential change of the 304SS electrodes coupled with the PTNRs film under intermittent visible light illumination. (b) The potential change of the 304SS electrodes coupled with the PTNRs film under 4 light on/off cycles. The SEM (c) and TEM (d) images of the PTNRs film, which was used in the above stability evaluation experiments for 8 h under intermittent visible light illumination.

304SS coupled with pure TNRs film, indicating that the PTNRs with core-shell structure can separate  $e^-/h^+$  pairs and transfer charges more effectively. Consequently, the PCP efficiency for 304SS can be further improved.

### 3.3. The stability evaluation of PTNRs film in PCP system of 304SS

As shown in Fig. 10a, the dark-state PCP efficiency of 304SS coupled with PTNRs is investigated under intermittent visible light illumination. After connecting with the PTNRs film, the 304SS potential negatively shifts to about -270 mV vs. Ag/AgCl before irradiation due to the galvanic effect. When provided with visible light illumination, the potential rapidly dropped to -630 mV vs. Ag/AgCl, which is consistent with the above results. After cutting off light (for 1 h illumination of visible light), the OCP of the 304SS shifted firstly to -330 mV vs. Ag/AgCl lower than the initial potential (-270 mV vs. Ag/AgCl). And then the potential of the 304SS connected to the PTNRs film increases slowly to the initial level as before irradiation, implying that this composite film can provide certain degree of delay protection even when the light source is turned off during this period (about 6 h). Meanwhile, to evaluate the potential-response stability of PTNRs film in the PCP system, the surface potential changes of the 304SS connected to this photoanode to the light on/off cycles were measured (as displayed in Fig. 10b). The results demonstrate that the PTNRs film can provide reproducible cathodic protection for 304SS, and the surface potential (around 290 mV vs. Ag/AgCl) of 304SS is still lower than its initial potential (around 270 mV vs. Ag/AgCl) and corrosion potential after 8 h' intermittent visible light illumination, showing high stability of the prepared films.

Based on the results mentioned above, the core-shell structure of PTNRs is the key point of the excellent cathodic protection efficiency against corrosion of 304SS, thus, it is of great value to investigate the structure stability of PTNRs film after PCP experiment. SEM and TEM images of PTNRs film used in the above stability evolution experiment, are displayed in Fig. 10c-d. It can be seen that the 1D electron transmission shortcut of nanorods are almost intact, still vertical to the FTO substrate. On the other hand, the coaxial structure of PTNRs is well sustained and the PPy layer still remain its initial thickness about 12.96

nm, showing the strong structural sustainability of PPy layer, which can further explain the PCP application potential of PTNRs film.

In the PCP system for 304SS, the  $S^{2-}$  in the electrolyte of the photoelectrochemical cell plays an important role to consume  $h^+$  (Eq. (2)), so as to promote the separation of  $e^-/h^+$  pairs and further improve the cathodic protection efficiency [22]. However, as an insulator, the generated elemental sulfur (S) may deposit onto the surface of photoanode to hinder the charge mobility of this film [26]. Fig. 11 displays the high resolution XPS spectrum of S 2p of PTNRs film after PCP experiment. The two strong peaks located at 168.77 eV and 169.97 eV with an energy band of 1.20 eV, is assigned to S 2p<sub>3/2</sub> and S 2p<sub>1/2</sub>, respectively, which can be ascribed to the sulfate ions ( $SO_4^{2-}$ ) [67]. However, there is no characteristic peaks for elemental S, implying that the generated elemental S forms dissolvable polysulfide ions and finally dissolve in the electrolyte solution, according to Eqs. (3) and (4) [68]. In a word, the elemental S generated by the oxidation of  $S^{2-}$  does not deposit onto the surface of photoanode, and impact little on the

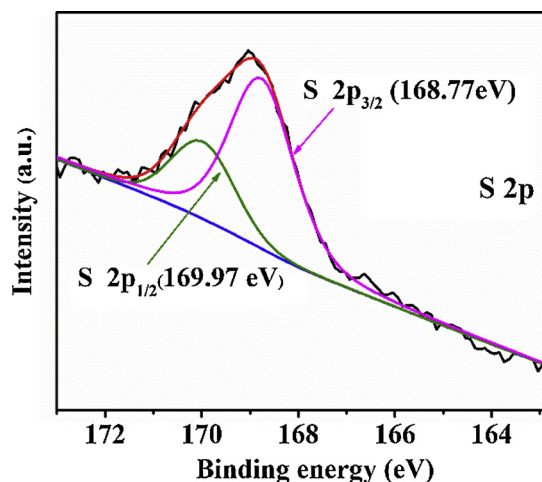


Fig. 11. The high resolution XPS spectrum of S 2p of the PTNRs film after PCP measurement.



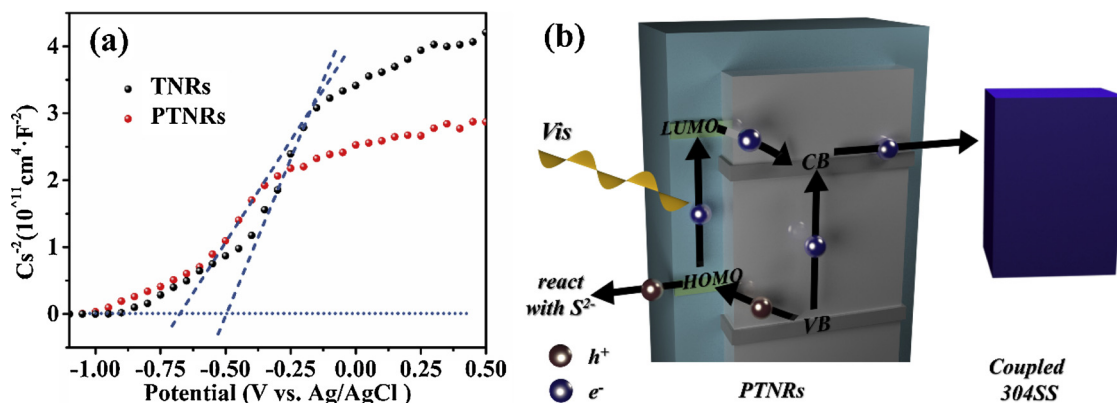
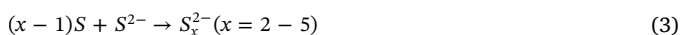


Fig. 12. (a) Mott-Schottky plots of TNRs and PTNRs films. (b) The sketch of the proposed charge photogeneration and transfer mechanism in the PTNRs film for the PCP application.

cathodic protection efficiency.



### 3.4. Mechanism

In order to further understand the PCP mechanism of PTNRs film for 304SS, the Mott-Schottky plots of TNRs and PTNRs films were tested (Fig. 12a). It can be seen that the flat band potential of PTNRs film is more negative than that of TNRs film. This indicates that the matched band alignment between  $TiO_2$  and PPY is formed after the deposition of PPY layer, and it is beneficial to the separation of  $e^-/h^+$  pairs and then hinders the recombination [69]. Additionally, there is a negative correlation between the charge density and the slope of Mott-Schottky plot [70]. The curve slope of PTNRs film is more negative than that of TNRs film, indicating a higher free carrier density of PTNRs, and exhibiting its superior photoelectrochemical performance. To sum up, the proposed charge photogeneration and immigration mechanism are displayed in Fig. 12b. When PTNRs film is irradiated by visible light, the p-type semiconductor of PPY with relatively narrow  $E_g$  of 2.2 eV, is excited [71]. A large number of generated electrons jump from PPY HOMO to PPY LUMO, and then flow directly into the  $TiO_2$  CB through the well-defined interface, as the  $TiO_2$  CB is more positive than the PPY LUMO [72]. Simultaneously, a few electrons are excited in  $TiO_2$  valence band (VB) and jump into  $TiO_2$  CB. All the photogenerated electrons immediately reach the coupled 304SS through FTO substrate, leading to a reduced surface potential of coupled metal, and the steel corrosion is effectively inhibited consequently. The  $h^+$  assembled in PPY HOMO in the opposite direction is consumed at the photoanode/electrolyte interface by  $S^{2-}$  according to the above oxidation reaction (Eqs. (2)–(4)). Compared with the TNRs film, the PTNRs film with the presence of p-n heterojunction, exhibits superior visible-light absorption capacity and higher separation efficiency of  $e^-/h^+$  pairs. Moreover, the residual electrons located at PPY LUMO are stored under visible light irradiation, and then released to the coupled 304SS in the dark condition (as mentioned in the above release mechanism Fig. S3), which indicates that this kind of films can provide sustain cathodic protection for the steel in the darkness.

### 4. Conclusion

In this study, PTNRs array film with core-shell structure was successfully prepared by electropolymerization method. The deposition of PPY layer onto single crystalline rutile TNRs array film can form

important p-n heterojunction. Compared with pure TNRs, PTNRs have higher visible light absorption ability and separation efficiency of  $e^-/h^+$  pairs, and can exhibit excellent photoelectrochemical performances based on core-shell structure. With visible light irradiation, the composite film can achieve a superior PCP performance for 304SS in 0.5 mol·L<sup>-1</sup> NaCl solution than the pure TNRs array film. What's more, the composite film can provide continuous cathodic protection due to the charge storage ability of PPY after light source is turned off. Therefore, PTNRs array film can be served as a potential photoanode material in the PCP applications for 304SS.

### Author contributions

Yunpeng Liu, Chengcheng Zhao and Xi Wang conceived and designed the work; Yunpeng Liu, Chengcheng Zhao, Hao Xu, and Hui Wang performed the experiments and characterizations; Yunpeng Liu wrote the manuscript; Yunpeng Liu, Hui Wang, Xuyang Zhao, Jiangtao Feng, Wei Yan and Zijun Ren analyzed the data and revised the manuscript. All authors have given approval to the final version of the manuscript.

### Declaration of Competing Interest

We declare that we do not have any commercial or associative interest that represents a conflict of interest in connection with the work submitted.

### Acknowledgements

The authors gratefully acknowledge the Shaanxi Key research and development projects, China (Grant No. 2017SF-386), the financial supports from the National Natural Science Foundation of China (Grant No. 21307098 and 21507104) and the Fundamental Research Funds for the Central Universities of China.

### Appendix A. Supplementary data

Supplementary material related to this article can be found, in the online version, at doi:<https://doi.org/10.1016/j.materresbull.2019.110751>.

### References

- [1] Y. Tsutsumi, A. Nishikata, T. Tsuru, Pitting corrosion mechanism of Type 304 stainless steel under a droplet of chloride solutions, *Corros. Sci.* 49 (2007) 1400–1407.
- [2] S. Mirhashemihaghghi, J. Światowska, V. Maurice, A. Seyeux, L.H. Klein, E. Salmi, M. Ritala, P. Marcus, Interfacial native oxide effects on the corrosion protection of copper coated with ALD alumina, *Electrochim. Acta* 193 (2016) 7–15.

- [3] M. Finšgar, J. Jackson, Application of corrosion inhibitors for steels in acidic media for the oil and gas industry: a review, *Corros. Sci.* 86 (2014) 17–41.
- [4] M. Dai, J. Liu, F. Huang, Y. Zhang, Y.F. Cheng, Effect of cathodic protection potential fluctuations on pitting corrosion of X100 pipeline steel in acidic soil environment, *Corros. Sci.* 143 (2018) 428–437.
- [5] M.C. Li, S.Z. Luo, P.F. Wu, J.N. Shena, Photocathodic protection effect of TiO<sub>2</sub> films for carbon steel in 3% NaCl solutions, *Electrochim. Acta* 50 (2005) 3401–3406.
- [6] H. Li, X. Wang, Q. Wei, X. Liu, Z. Qian, B. Hou, Enhanced photocathodic protection performance of Ag/graphene/TiO<sub>2</sub> composite for 304SS under visible light, *Nanotechnology* 28 (2017) 225701–225708.
- [7] T. Jian, Z. Zhenhuan, K. Anil, R.I. Boughton, L. Hong, Recent progress in design, synthesis, and applications of one-dimensional TiO<sub>2</sub> nanostructured surface heterostructures: a review, *Chem. Soc. Rev.* 43 (2014) 6920–6937.
- [8] L. Kiyoun, M. Anca, S. Patrik, One-dimensional titanium dioxide nanomaterials: nanotubes, *Chem. Rev.* 114 (2014) 9385.
- [9] X.T. Wang, X.B. Ning, Q. Shao, S.S. Ge, Z.Y. Fei, J. Lei, B.R. Hou, ZnFeAl-layered double hydroxides/TiO<sub>2</sub> composites as photoanodes for photocathodic protection of 304 stainless steel, *Sci. Rep.* 8 (2018) 4116–4124.
- [10] Y.F. Zhu, Photogenerated cathodic protection properties of a TiO<sub>2</sub> nanowire film prepared by a hydrothermal method, *Acta Phys. Chim. Sin.* 26 (2010) 2349–2353.
- [11] W. Sun, N. Wei, H. Cui, Y. Lin, X. Wang, J. Tian, J. Li, J. Wen, 3D ZnIn<sub>2</sub>S<sub>4</sub> nanosheet/TiO<sub>2</sub> nanowire arrays and their efficient photocathodic protection for 304 stainless steel, *Appl. Surf. Sci.* 434 (2018) 1030–1039.
- [12] Q. Shen, Y. Wang, J. Xue, G. Gao, X. Liu, H. Jia, Q. Li, B. Xu, The dual effects of RGO films in TiO<sub>2</sub>/CdSe heterojunction: enhancing photocatalytic activity and improving photocorrosion resistance, *Appl. Surf. Sci.* 481 (2019) 1515–1523.
- [13] M. Yang, L. Zhang, B. Jin, L. Huang, Y. Gan, Enhanced photoelectrochemical properties and water splitting activity of self-ordered MoO<sub>3</sub>-TiO<sub>2</sub> nanotubes, *Appl. Surf. Sci.* 364 (2016) 410–415.
- [14] K. Zhu, N.R. Neale, A. Miedaner, A.J. Frank, Enhanced charge-collection efficiencies and light scattering in dye-sensitized solar cells using oriented TiO<sub>2</sub> nanotubes arrays, *Nano Lett.* 7 (2007) 69–74.
- [15] G.K. Mor, K. Shankar, M. Paulose, O.K. Varghese, C.A. Grimes, Use of highly-ordered TiO<sub>2</sub> nanotube arrays in dye-sensitized solar cells, *Nano Lett.* 6 (2006) 215–218.
- [16] L. Bin, E.S. Aydil, Growth of oriented single-crystalline rutile TiO<sub>2</sub> nanorods on transparent conducting substrates for dye-sensitized solar cells, *J. Am. Chem. Soc.* 131 (2009) 3985–3990.
- [17] J. Hu, Z.C. Guan, Y. Liang, J.Z. Zhou, Q. Liu, H.P. Wang, H. Zhang, R.G. Du, Bi<sub>2</sub>S<sub>3</sub> modified single crystalline rutile TiO<sub>2</sub> nanorod array films for photoelectrochemical cathodic protection, *Corros. Sci.* 125 (2017) 59–67.
- [18] S. Zuo, Z. Liu, W. Liu, X. Li, Z. Li, C. Yao, Q. Chen, Y. Fu, TiO<sub>2</sub> nanorod arrays on the conductive mica combine photoelectrochemical cathodic protection with barrier properties, *J. Alloys Compd.* 776 (2019) 529–535.
- [19] H. Wan, W. Yao, W. Zhu, Y. Tang, H. Ge, X. Shi, T. Duan, Fe-N co-doped SiO<sub>2</sub>@TiO<sub>2</sub> yolk-shell hollow nanospheres with enhanced visible light photocatalytic degradation, *Appl. Surf. Sci.* 444 (2018) 355–363.
- [20] X. Li, X. Wang, X. Ning, J. Lei, J. Shao, W. Wang, Y. Huang, B. Hou, Sb<sub>2</sub>S<sub>3</sub>/Sb<sub>2</sub>O<sub>3</sub> modified TiO<sub>2</sub> photoanode for photocathodic protection of 304 stainless steel under visible light, *Appl. Surf. Sci.* 462 (2018) 155–163.
- [21] J. Zhang, Z. Ur Rahman, Y. Zheng, C. Zhu, M. Tian, D. Wang, Nanoflower like SnO<sub>2</sub>-TiO<sub>2</sub> nanotubes composite photoelectrode for efficient photocathodic protection of 304 stainless steel, *Appl. Surf. Sci.* 457 (2018) 516–521.
- [22] Z.C. Guan, X. Wang, P. Jin, Y.Y. Tang, H.P. Wang, G.L. Song, R.G. Du, Enhanced photoelectrochemical performances of ZnS-Bi<sub>2</sub>S<sub>3</sub>/TiO<sub>2</sub>/WO<sub>3</sub> composite film for photocathodic protection, *Corros. Sci.* 143 (2018) 31–38.
- [23] J. Zhang, R.G. Du, Z.Q. Lin, Y.F. Zhu, Y. Guo, H.Q. Qi, L. Xu, C.J. Lin, Highly efficient CdSe/CdS co-sensitized TiO<sub>2</sub> nanotube films for photocathodic protection of stainless steel, *Electrochim. Acta* 83 (2012) 59–64.
- [24] J.M. Kim, S.H. Yun, H.J. Kim, K. Song, S.H. Kim, H.S. Park, Hollow triple-shelled SiO<sub>2</sub>/TiO<sub>2</sub>/polypyrrole nanospheres for enhanced lithium storage capability, *Chem. Eng. J.* 237 (2014) 380–386.
- [25] S. Cui, X. Yin, Q. Yu, Y. Liu, D. Wang, F. Zhou, Polypyrrole nanowire/TiO<sub>2</sub> nanotube nanocomposites as photoanodes for photocathodic protection of Ti substrate and 304 stainless steel under visible light, *Corros. Sci.* 98 (2015) 471–477.
- [26] J. Ren, B. Qian, J. Li, Z. Song, L. Hao, J. Shi, Highly efficient polypyrrole sensitized TiO<sub>2</sub> nanotube films for photocathodic protection of Q235 carbon steel, *Corros. Sci.* 111 (2016) 596–601.
- [27] Z.D. Ni, Y.T. Song, H.Q. Chen, L.Y. Lin, UV light-assisted electropolymerization of Pyrrole on TiO<sub>2</sub> for supercapacitors: investigating the role of TiO<sub>2</sub>, *Electrochim. Acta* 190 (2016) 313–321.
- [28] L. Jie, M. Yi, H. Wang, J. Chen, Preparation of polypyrrole sensitized TiO<sub>2</sub> nanotube arrays hybrids for efficient photoelectrochemical water splitting, *Electrochim. Acta* 167 (2015) 119–125.
- [29] W. Zheng, X. Li, C. Dong, X. Yan, G. He, Fabrication of a visible light detector based on a coaxial polypyrrole/TiO<sub>2</sub> nanorod heterojunction, *RSC Adv.* 4 (2014) 44868–44871.
- [30] Y. Oaki, T. Oki, H. Imai, Enhanced photoconductive properties of a simple composite coaxial nanostructure of zinc oxide and polypyrrole, *J. Mater. Chem.* 22 (2012) 21195–21200.
- [31] N. Wei, Y. Liu, M. Feng, Z. Li, S. Chen, Y. Zheng, D. Wang, Controllable TiO<sub>2</sub> core-shell phase heterojunction for efficient photoelectrochemical water splitting under solar light, *Appl. Catal. B* 244 (2019) 519–528.
- [32] Y. Wang, X. Zhan, F. Wang, Q. Wang, S. Muhammad, J. He, J. Mater, Y. Wang, X. Zhan, F. Wang, Crystalline ZnO/ZnS<sub>x</sub>Se<sub>1-x</sub> core-shell nanowire arrays for efficient visible-light photoelectrocatalysis, *J. Mater. Chem. A* 2 (2014) 18413–18419.
- [33] L.K. Dhandole, M.A. Mahadik, H.-S. Chung, W.-S. Chae, M. Cho, J.S. Jang, CdIn<sub>2</sub>S<sub>4</sub> chalcogenide/TiO<sub>2</sub> nanorod heterostructured photoanode: an advanced material for photoelectrochemical applications, *Appl. Surf. Sci.* 490 (2019) 18–29.
- [34] P. Soundarrajan, K. Sankarasubramanian, T. Logu, K. Sethuraman, K. Ramamurthi, Growth of rutile TiO<sub>2</sub> nanorods on TiO<sub>2</sub> seed layer prepared using facile low cost chemical methods, *Mater. Lett.* 116 (2014) 191–194.
- [35] H.L. Ma, J.Y. Yang, Y. Dai, Y.B. Zhang, B. Lu, G.H. Ma, Raman study of phase transformation of TiO<sub>2</sub> rutile single crystal irradiated by infrared femtosecond laser, *Appl. Surf. Sci.* 253 (2007) 7497–7500.
- [36] N. Maráková, P. Humpolíček, V. Kašpárková, Z. Zapáková, L. Martinková, P. Bober, M. Trchová, J. Stejskal, Antimicrobial activity and cytotoxicity of cotton fabric coated with conducting polymers, polyaniline or polypyrrole, and with deposited silver nanoparticles, *Appl. Surf. Sci.* 396 (2017) 169–176.
- [37] J. Upadhyay, A. Kumar, B. Gogoi, A.K. Buragohain, Biocompatibility and anti-oxidant activity of polypyrrole nanotubes, *Synth. Met.* 189 (2014) 119–125.
- [38] H.-f. Jin, T. Wang, J. Deng, Growth of branched rutile TiO<sub>2</sub> nanorod arrays on F-doped tin oxide substrate, *Appl. Surf. Sci.* 257 (2011) 10494–10498.
- [39] M. Irshad, M.A. Khan, S.A. Khan, I. Ali, G. Murtaza, M.N. Ashiq, A. Aziz, A. Manzoor, Improved electrical, magnetic and dielectric properties of polypyrrole (PPy) substituted spinel ferrite composites, *Phys. E (Amsterdam, Neth.)* 93 (2017) 313–317.
- [40] S. Kment, F. Riboni, S. Pausova, L. Wang, L. Wang, H. Han, Z. Hubicka, J. Krysa, P. Schmuk, R. Zboril, Photoanodes based on TiO<sub>2</sub> and alpha-Fe<sub>2</sub>O<sub>3</sub> for solar water splitting - superior role of 1D nanoarchitectures and of combined heterostructures, *Chem. Soc. Rev.* 46 (2017) 3716–3769.
- [41] T. Kubo, A. Nakahira, Local structure of TiO<sub>2</sub>-Derived nanotubes prepared by the hydrothermal process, *J. Phys. Chem. C* 112 (2008) 1658–1662.
- [42] W. Cui, J. He, H. Wang, J. Hu, L. Liu, Y. Liang, Polyaniline hybridization promotes photo-electro-catalytic removal of organic contaminants over 3D network structure of rGH-PANI/TiO<sub>2</sub> hydrogel, *Appl. Catal. B* 232 (2018) 232–245.
- [43] H. Liu, W. Yang, M. Ying, Y. Cao, J. Yao, Z. Jing, T. Hu, Synthesis and characterization of titania prepared by using a photoassisted sol-gel method, *Langmuir* 19 (2003) 3001–3005.
- [44] Y. Liu, W. Zhang, C. Zhao, H. Wang, J. Chen, L. Yang, J. Feng, W. Yan, Study on the synthesis of poly(pyrrole methanes) with the hydroxyl in different substituent position and their selective adsorption for Pb<sup>2+</sup>, *Chem. Eng. J.* 361 (2019) 528–537.
- [45] M.M. Momeni, Y. Ghayeb, N. Moosavi, Preparation of Ni-Pt/Fe-TiO<sub>2</sub> nanotube films for photoelectrochemical cathodic protection of 403 stainless steel, *Nanotechnology* 29 (2018) 425701–425708.
- [46] Z. Jinfeng, Z. Peng, L. Jianjun, Y. Jiaguo, New understanding of the difference of photocatalytic activity among anatase, rutile and brookite TiO<sub>2</sub>, *Phys. Chem. Phys.* 16 (2014) 20382–20386.
- [47] Z. Yu, D.T. Payne, C.L. Pang, H.H. Fielding, G. Thornton, Non-band-gap photo-excitation of hydroxylated TiO<sub>2</sub>, *J. Phys. Chem. Lett.* 6 (2015) 3391–3395.
- [48] N. Serpone, D. Lawless, R. Khairutdinov, Size effects on the photophysical properties of colloidal anatase TiO<sub>2</sub> particles: size quantization versus direct transitions in this indirect semiconductor? *J. Phys. Chem.* 99 (1995) 16646–16654.
- [49] M. Meksi, A. Turki, H. Kochkar, L. Bousselmi, C. Guillard, G. Berhault, The role of lanthanum in the enhancement of photocatalytic properties of TiO<sub>2</sub> nanomaterials obtained by calcination of hydrogenotitanate nanotubes, *Appl. Catal. B* 181 (2016) 651–660.
- [50] M. Hamandi, G. Berhault, C. Guillard, H. Kochkar, Reduced graphene oxide/TiO<sub>2</sub> nanotubes composites for formic acid photodegradation, *Appl. Catal. B* 209 (2017) 203–213.
- [51] Y. Yang, W. Cheng, Y.F. Cheng, Preparation of Co<sub>3</sub>O<sub>4</sub>@ZnO core-shell nanocomposites with intrinsic p-n junction as high-performance photoelectrodes for photoelectrochemical cathodic protection under visible light, *Appl. Surf. Sci.* 476 (2019) 815–821.
- [52] M. Tammer, Spectroscopic Ellipsometry on Thin Films of Conjugated Polymers, Durham university, 2001.
- [53] X.B. Ning, S.S. Ge, X.T. Wang, H. Li, X.R. Li, X.Q. Liu, Y.L. Huang, Preparation and photocathodic protection property of Ag<sub>2</sub>S-TiO<sub>2</sub> composites, *J. Alloys Compd.* 719 (2017) 15–21.
- [54] H. Li, X. Wang, L. Zhang, B. Hou, Preparation and photocathodic protection performance of CdSe/reduced graphene oxide/TiO<sub>2</sub> composite, *Corros. Sci.* 94 (2015) 342–349.
- [55] X. Cheng, H. Liu, Q. Chen, J. Li, W. Pu, Preparation of CdS NCs decorated TiO<sub>2</sub> nanotubes arrays photoelectrode and its enhanced photoelectrocatalytic performance and mechanism, *Electrochim. Acta* 105 (2013) 535–541.
- [56] C. Lei, L. Yu, Z. Han, Z. Feng, R. Du, Photogenerated cathodic protection of stainless steel by liquid-phase-deposited sodium polyacrylate/TiO<sub>2</sub> hybrid films, *Corros. Sci.* 68 (2013) 214–222.
- [57] D.A. W, Y. Liu, C.W. Wang, F. Zhou, W.M. Liu, Highly flexible coaxial nanohybrids made from porous TiO<sub>2</sub> nanotubes, *ACS Nano* 3 (2009) 1249–1257.
- [58] M.M. Momeni, M. Mahvari, Y. Ghayeb, Photoelectrochemical properties of iron-cobalt WTiO<sub>2</sub> nanotube photoanodes for water splitting and photocathodic protection of stainless steel, *J. Electroanal. Chem.* 832 (2019) 7–23.
- [59] Q. Wei, X. Wang, X. Ning, X. Li, J. Shao, H. Li, W. Wang, Y. Huang, B. Hou, Characteristics and anticorrosion performance of WSe<sub>2</sub>/TiO<sub>2</sub> nanocomposite materials for 304 stainless steel, *Surf. Coat. Technol.* 352 (2018) 26–32.
- [60] W. Sun, S. Cui, N. Wei, S. Chen, Y. Liu, D. Wang, Hierarchical WO<sub>3</sub>/TiO<sub>2</sub> nanotube nanocomposites for efficient photocathodic protection of 304 stainless steel under visible light, *J. Alloys Compd.* 749 (2018) 741–749.
- [61] W. Liu, T. Du, Q. Ru, S. Zuo, Y. Cai, C. Yao, Preparation of graphene/WO<sub>3</sub>/TiO<sub>2</sub> composite and its photocathodic protection performance for 304 stainless steel, *Mater. Res. Bull.* 102 (2018) 399–405.

- [62] N. Wei, Y. Liu, T. Zhang, J. Liang, D. Wang, Hydrogenated TiO<sub>2</sub> nanotube arrays with enhanced photoelectrochemical property for photocathodic protection under visible light, *Mater. Lett.* 185 (2016) 81–84.
- [63] A. Boonserm, C. Kruehong, V. Seiththanabutra, A. Artnaseaw, Photoelectrochemical response and corrosion behavior of CdS/TiO<sub>2</sub> nanocomposite films in an aerated 0.5 M NaCl solution, *Appl. Surf. Sci.* 419 (2017) 933–941.
- [64] L. Hong, X. Wang, L. Yi, B. Hou, Ag and SnO<sub>2</sub> co-sensitized TiO<sub>2</sub> photoanodes for protection of 304SS under visible light, *Corros. Sci.* 82 (2014) 145–153.
- [65] L. Xu, Y.F. Zhu, J. Hu, J. Zhang, C.J. Lin, TiO<sub>2</sub> nanotube films prepared by anodization in glycerol solutions for photocathodic protection of stainless steel, *J. Electrochem. Soc.* 161 (2014) C231–C235.
- [66] T. Zhang, Y. Liu, J. Liang, D. Wang, Enhancement of photoelectrochemical and photocathodic protection properties of TiO<sub>2</sub> nanotube arrays by simple surface UV treatment, *Appl. Surf. Sci.* 394 (2017) 440–445.
- [67] R.P.W.J. Struis, T.J. Schildhauer, I. Czekaj, M. Janousch, S.M.A. Biollaz, C. Ludwig, Sulphur poisoning of Ni catalysts in the SNG production from biomass: a TPO/XPS/XAS study, *Appl. Catal. A Gen.* 362 (2009) 121–128.
- [68] A.A., Electrochemical production of hydrogen and sulfur by low-temperature decomposition of hydrogen sulfide in an aqueous alkaline solution, *J. Electrochem. Soc.* 137 (1990) 2703–2709.
- [69] H. Zhu, M. Zhao, J. Zhou, W. Li, H. Wang, X. Zhe, L. Lei, P. Lang, S. Zhan, S. Yan, Surface states as electron transfer pathway enhanced charge separation in TiO<sub>2</sub> nanotube water splitting photoanodes, *Appl. Catal. B* (2018) 100–108.
- [70] X. Wang, J. Lei, Q. Shao, X. Li, X. Ning, J. Shao, J. Duan, B. Hou, Preparation of ZnWO<sub>4</sub>/TiO<sub>2</sub> composite film and its photocathodic protection for 304 stainless steel under visible light, *Nanotechnology* 30 (2018) 5710–5716.
- [71] L.I. Xiangcun, G. Jiang, H.E. Gaohong, W. Zheng, Y.I. Tan, W.U. Xiao, Preparation of porous PPy-TiO<sub>2</sub> composites: improved visible light photoactivity and the mechanism, *Chem. Eng. J.* 236 (2014) 480–489.
- [72] C. Zhang, W. Bai, Z. Yang, A novel photoelectrochemical sensor for bilirubin based on porous transparent TiO<sub>2</sub> and molecularly imprinted polypyrrole, *Electrochim. Acta* 187 (2016) 451–456.